2024 IEEE/RSJ International Conference on Intelligent Robots and Systems (IROS)
October 14-18, 2024. Abu Dhabi, UAE

An MR Safe Double-Arch Needle Insertion Robot with Scissor-Folding Mechanism for Abdominal Percutaneous Interventions*

Ziting Liang[1], Chuang Lu[1], Haoqian Yang[1], Ryman Hashem[1], Mohamed E.M.K. Abdelaziz[3], Lukas Lindenroth[2], Steve Bandula[1,4], Danail Stoyanov[1], and Agostino Stilli[1]

***Abstract*— Tumors affecting abdominal organs rank among the deadliest malignancies. In this context, Magnetic Resonance Imaging (MRI) serves as an effective diagnostic tool with a strong potential to support image-guided minimally invasive interventions for treating these tumours, offering an ionizing-radiation-free medical modality. MRI provides exceptional soft tissue contrast and multi-angle imaging, enabling accurate intraoperative localisation of target tumours within these vital organs. Nevertheless, MRI-guided minimally invasive interventions still encounter significant challenges due to the strong magnetic field environment and the narrow and deep bore of MRI machines. This paper proposes a novel MR safe 5-degrees-of-freedom (DoFs) parallel table-mounted double-arch needle insertion robot with a scissor-folding mechanism (SFM) for abdominal interventions. The proposed robot is designed to fit a standard 70-cm MRI bore. Initial evaluation experiments indicate mean errors of 3.14 mm for the proposed robotic arch and 2.23 mm for the full needle insertion robot, respectively. Additionally, preliminary testing of the system in an MRI environment resulted in unaltered MRI imaging output, with negligible artefacts associated with the presence of the robot within the bore.**

I. INTRODUCTION

Cancers that develop in the abdominal organs pose a substantial threat to human life. For example, liver cancer alone resulted in an estimated 830,000 deaths in 2020, ranking as the third leading cause of cancer mortality worldwide [1]. There were also more than 430,000 new cases of kidney cancer in 2020 globally [2]. While traditional surgical approaches remain a critical modality, advancements in medical research have significantly improved the treatment methods. Among these innovations, image-guided minimally invasive percutaneous interventions have notably emerged as effective means to eliminate tumour tissue in hard-to-reach locations within abdominal organs. These interventions rely on various forms of ablation, such as cryoablation, radiofrequency ablation (RFA), and microwave ablation. This minimally invasive approach offers reduced perioperative complications and shorter recovery times, particularly for treating tumours located in organs such as the liver and kidney. In image-guided minimally invasive percutaneous interventions, both computerized tomography (CT) and ultrasound (US) imaging techniques are commonly employed by surgeons to precisely navigate the needle probe to the target tissue location. Differently, MRI has been scarcely applied in these surgical procedures despite being one of the most advanced medical imaging technologies available, with advantages such as unparalleled soft tissue contrast, versatile imaging from multiple angles, and the critical advantage of being free from ionising radiation [3]. The primary challenges hindering the employment of MRI-guided techniques include the limited operating space for the surgeons due to the confined bore of the MRI scanner [4] and limited availability of MRI-compatible surgical instruments needed to prevent damages to the machine as well as electromagnetic interference that can potentially degrade the quality of the images collected.

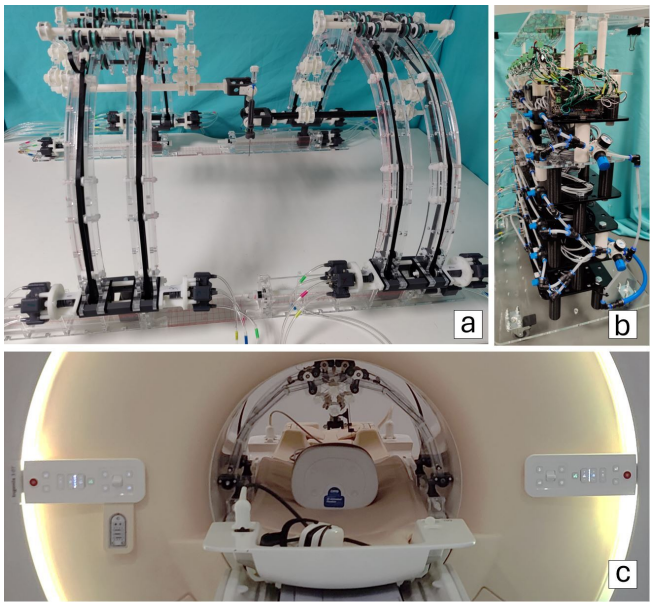

Fig. 1: Proposed needle insertion robot on a table (a), the tower control platform (b) and (c) the robot within MRI scanner

With the progression in medical robotics, the development of MRI-compatible robots, designed to function as an assistant in surgical procedures, where systems are directly guided by the surgeon, could potentially overcome the challenges

*This research was funded by the Wellcome/EPSRC Centre for Interventional and Surgical Sciences (WEISS) [203145/Z/16/Z]; the Engineering and Physical Sciences Research Council (EPSRC) [EP/P027938/1, EP/R004080/1, EP/P012841/1] and the Royal Academy of Engineering Chair in Emerging Technologies Scheme [CiET1819/2/36]. For the purpose of open access, the authors have applied a CC BY public copyright licence to any Author Accepted Manuscript version arising from this submission

[1]Wellcome/EPSRC Centre for Interventional and Surgical Sciences, University College London, WC1E 6BT London, UK a.stilli@ucl.ac.uk

[2]School of Biomedical Engineering and Imaging Sciences, King's College London, SE1 7EU, London, UK

[3]The Hamlyn Centre, Imperial College London, SW7 2AZ, London, UK

[4]Interventional Oncology Service, University College London Hospital, NW1 2BU London, UK

previously outlined. Based on their setup configurations, these robots can be primarily categorised into three types: ground-based [5], tabled-mounted [6], and body-mounted [7]. The primary advantage of ground-based robots lies in their mobility, such as [8]. However, this type of robot can be quite bulky, and they often employ long, multi-jointed mechanical arms. Combined with the material constraints imposed by the MRI environment, these robots come with exceptionally high requirements in terms of the robustness and rigidity of their mechanical structures, as well as the precision of positioning. By contrast, body-mounted robots such as [9] boast compact designs and can compensate for the impact of respiratory motion on needle insertion towards the target location [10]. However, when attached to the body of a patient, such as by using straps, these robots often face stability challenges, and the tolerance of weight they impose on patients becomes a critical concern. Table-mounted robots provide a balanced approach to the footprint of the robot, allowing for their installation within the scanning bore and secured to the scanning table while preserving the essential space for patient examinations.

Franco *et al.* developed a table-mounted robot with a hybrid serial-parallel structure using pneumatic cylinders for MRI-guided laser ablation of liver tumours [6]. This robot, designed as a flat platform with a gantry to secure the pneumatic cylinders and mount the pneumatic actuators that facilitate translational motion, occupies a significant portion of the volume of the MRI scanning bore. Christoforou *et al.* [11] developed a robot featuring an arch structure and five DoFs, yet its manual actuation presents challenges in integrating online planning tools for semi-autonomous tasks, including needle insertion. Alvara *et al.* [12] developed a robot powered by ultrasonic rotary motors for bone biopsies with an arch structure and multi-revolute joints. In that work, the actuation method of the multi-revolute joints sliding along the arch is not comprehensively addressed and the volume occupied by these joints remains a significant concern. Researchers from Johns Hopkins University have developed MRI-conditional body-mounted robots featuring scissor mechanisms for MRI-guided percutaneous interventions [13], [14]. The compact design of these foldable scissor mechanisms minimises space occupation while allowing for component extension. Nonetheless, the implementation of scissor mechanisms driven by several rotating discs may present challenges in table-mounted configurations where the patients are situated below the robots.

For the requirements of MRI-compatible robot, the predominant standard for medical devices used in MRI is ASTM F2503. MR safe item necessitates materials to be electrically non-conductive, nonmetallic, and nonmagnetic [15], and has emerged as a trend for such devices, as proposed in [16], [9], [17], [18]. In addition, a space analysis demonstrated that the distance between the skin of patients and the wall of the MRI scanner is approximately 20 cm within 60-cm scanning bores [11].

In this work, a novel table-mounted MR safe 5-DoF parallel robot with SFM is proposed. The system is presented in

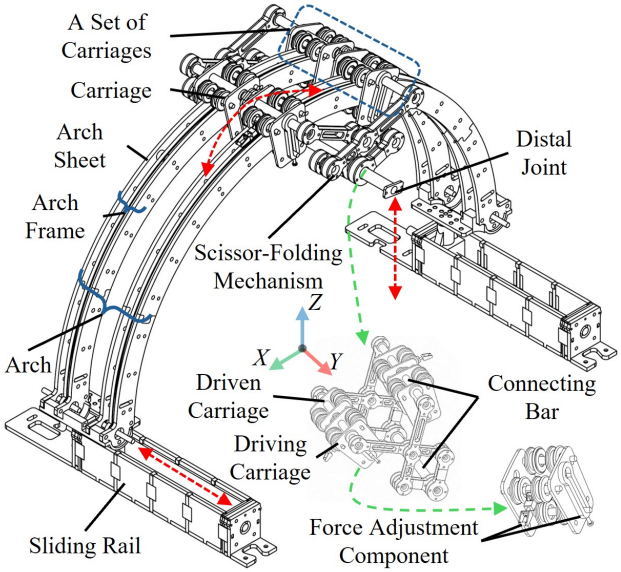

Fig. 2: Overview of the robotic arch and its components.

Fig. 1. The highlighting structure of the SFM, coupled with carriages that glide along the arch powered by the pneumatic motors positioned on either side, enables extension in the radial direction of the arches, while the arch itself can slide along the rails. This innovative approach further optimises the spatial utilisation within the scanning bore, ensuring that the patient can lie beneath the robot without any risk of interference. The bore opening diameters of MRI scanners may vary, generally spanning from 60 cm to 80 cm. The proposed robot is specifically designed for compatibility with the most commonly used wide-bore MRI scanners, featuring a 70-cm bore opening diameter. However, the design can be adapted to better fit larger and potentially smaller bores, with the highlight of accommodating patients with varying physiques and pursuing a larger workspace due to the arch and SFM architecture, which is specifically optimized for the cylindrical MRI scanning bore.

II. Methodology

A. Design of the Robotic Arch with Scissor-Folding Mechanism

In Fig. 2, the key module on which the proposed robot is based is presented. This robotic arch embeds an SFM mechanism, an arch, four carriages assembly and two sliding rails. The robotic arch incorporates two arch frames, providing a semicircular track for the carriages, and two sliding rails. Besides, the arch itself is capable of sliding along the sliding rails, which can be secured in the guides on both sides of the MRI scanner table that are typically used to secure the coils. As a result, a motion in the longitudinal direction of the MRI scanner, depicted as direction Y in the figure, can be achieved.

The carriage assembly, consisting of two sets of carriages, can glide along the arch to facilitate circular motion. Each set of carriages comprises one driving carriage and one driven carriage, with a connecting bar linking them. The

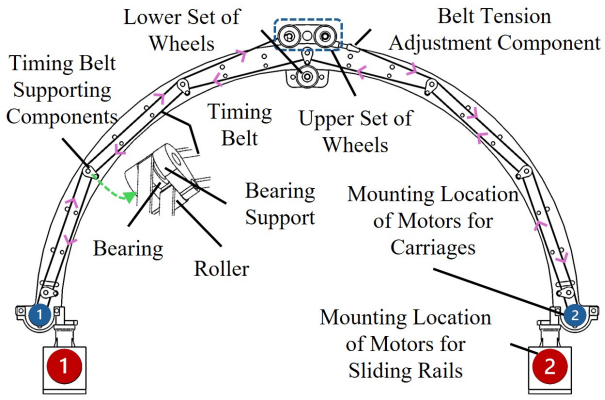

Fig. 3: Robotic arch actuation and transmission scheme

driving carriage features a timing belt tension adjustment component, while the driven carriage serves as an auxiliary unit to enhance the stability of the SFM. Besides, to ensure smooth gliding, each carriage is outfitted with two pairs of wheels contacting the arch sheets, as depicted in Fig. 3. Furthermore, a tension adjustment component and rubber rings are integrated to regulate the contact force between the wheels and the arch. Additionally, the timing belt is nestled between the gap of the two arch sheets in each arch frame to minimise occupancy.

The SFM, which comprises several interconnected bars, functions similarly to the opening and closing mechanism of scissors. The ends of the bars are affixed to the two sets of carriages, such that the carriages can drive the SFM to expand and contract. Therefore, the proposed SFM enables radial movement while significantly reducing the footprint within the constrained space of the MRI scanner bore.

The force and torque transmission scheme of the robot is described in the following sub-section. To prevent any possible interaction with the patients positioned underneath, it is crucial to ensure that the timing belts are confined within the arch. Besides, as MRI-compatible pneumatic motors always struggle to provide sufficient torque, the friction between the timing belts and their supporting components should be minimised. The winding method of the timing belt is illustrated in Fig.3. The number of support components has been optimised and strategically distributed along the arch to minimise the contact points with the timing belt while ensuring its proper confinement within the structure. Concurrently, the support components have employed a combination of bearings and rollers to guarantee smooth and unimpeded sliding. Furthermore, a multi-motor approach has been utilised to lower the torque demand on each motor, thus their individual encumbrance, and these motors are mounted on both sides of the robot.

B. Kinematics Analysis

The kinematic diagram of the arch structure with the SFM is illustrated in Fig.4. The robotic arch consists of four prismatic joints and six revolute joints. The centre point of the arch is defined as O of the system. The central plane of the arch structure is designated as plane α. The fixed connections between the arch and the sliding rails

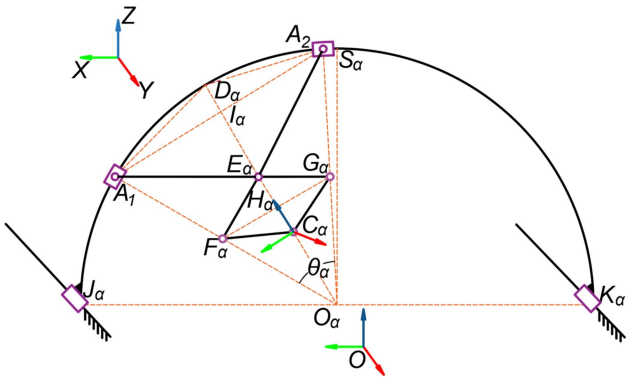

Fig. 4: Kinematic diagram of the robotic arch

are J_α and K_α. The connections between the two ends of the SFM and the arch are A_1 and A_2. The radius of the arch is R.S_α is the midpoint of $\overset{\frown}{J_\alpha K_\alpha}$. $l_{A_1G_\alpha}$, $l_{S_\alpha F_\alpha}$, $l_{F_\alpha C_\alpha}$ and $l_{G_\alpha C_\alpha}$ respectively represent the four bars of the SFM, while E_α and C_α denote the pivot points. The SFM is symmetrical about the line passing through O_α, C_α and E_α. Therefore, $l_{A_1G_\alpha}$ is equal to $l_{A_2E_\alpha}$, $l_{E_\alpha G_\alpha}$ is equal to $l_{E_\alpha F_\alpha}$, and $l_{F_\alpha C_\alpha}$ is equal to $l_{G_\alpha C_\alpha}$. Besides, D_α, I_α, H_α are the midpoint of $\overset{\frown}{A_1A_2}$, $l_{A_1A_2}$ and $l_{F_\alpha G_\alpha}$ respectively. The distance travelled by the arch along the sliding rails (Y direction) is d_{J_α} and d_{K_α}, where the d_{J_α} is equal to the d_{K_α}, while the rotation angles for the two sets of carriages are $\angle A_1O_\alpha J_\alpha$ as θ_{A_1} and $\angle A_2O_\alpha J_\alpha$ as θ_{A_2}, both starting from the direction of $\overrightarrow{O_\alpha J_\alpha}$. Overall, the input parameters of the robotic arch are $(d_{K_\alpha}, \theta_{A_1}, \theta_{A_2})$, and the output parameters are $(x_{C_\alpha}, y_{C_\alpha}, z_{C_\alpha}, \alpha_{C_\alpha}, \beta_{C_\alpha}, \gamma_{C_\alpha})$ where α, β, and γ donate the rotation along the axis X, Y, and Z respectively. Since the endpoint of the robotic arch is not able to rotate along axis X, Y, and Z, the DoF of the proposed robotic arch is $(x_{C_\alpha}, y_{C_\alpha}, z_{C_\alpha})$.

The forward kinematics of the proposed robotic arch are built in the subsequent section. $A_1\,(x_{A_1}, y_{A_1}, z_{A_1})$ and $A_2\,(x_{A_2}, y_{A_2}, z_{A_2})$ can be represented as $(R\cos\theta_{A_1}, d_{J_\alpha}, R\sin\theta_{A_1})$ and $(R\cos\theta_{A_2}, d_{J_\alpha}, R\sin\theta_{A_2})$. Therefore, $\angle I_\alpha O_\alpha J_\alpha$ and $I_\alpha\,(x_{I_\alpha}, y_{I_\alpha}, z_{I_\alpha})$ will be $\frac{\theta_{A_1}+\theta_{A_2}}{2}$, $\frac{A_1+A_2}{2}$. It can also be expressed as:

$$I_\alpha = \begin{bmatrix} \frac{R(\cos\theta_{A_1}+\cos\theta_{A_2})}{2} \\ d_{J_\alpha} \\ \frac{R(\sin\theta_{A_1}+\sin\theta_{A_2})}{2} \end{bmatrix} \tag{1}$$

Then, $\angle A_1E_\alpha I_\alpha$ can be calculated using the formula $\angle A_1E_\alpha I_\alpha = \arcsin\left(\frac{l_{A_1I_\alpha}}{l_{A_1E_\alpha}}\right)$, which is equal to:

$$\arcsin\left(\frac{R\sqrt{(\sin\theta_{A_1}-\sin\theta_{A_2})^2+(\cos\theta_{A_1}-\cos\theta_{A_2})^2}}{2l_{A_1E_\alpha}}\right) \tag{2}$$

Based on the triangular geometry, the following can be derived:

$$l_{I_\alpha E_\alpha} = \sqrt{l^2_{A_1E_\alpha} - l^2_{A_1I_\alpha}} \tag{3}$$

$$l_{E_\alpha H_\alpha} = l_{E_\alpha G_\alpha}\cos\angle A_1E_\alpha I_\alpha \tag{4}$$

$$l_{F_\alpha H_\alpha} = \sqrt{l^2_{E_\alpha F_\alpha} - l^2_{E_\alpha H_\alpha}} \tag{5}$$

$$l_{H_\alpha C_\alpha} = \sqrt{l^2_{F_\alpha C_\alpha} - l^2_{F_\alpha H_\alpha}} \tag{6}$$

Therefore, $\overrightarrow{|O_\alpha I_\alpha|}$ can be derived:

$$\begin{aligned} l_{I_\alpha C_\alpha} &= l_{I_\alpha E_\alpha} + l_{E_\alpha H_\alpha} + l_{H_\alpha C_\alpha} \\ &= \sqrt{l^2_{E_\alpha F_\alpha} \cos^2 \angle A_1 E_\alpha I_\alpha - l^2_{E_\alpha F_\alpha} + l^2_{F_\alpha C_\alpha}} \\ &+ l_{E_\alpha F_\alpha} \cos \angle A_1 E_\alpha I_\alpha \\ &+ \sqrt{l^2_{A_1 E_\alpha} - l^2_{A_1 I_\alpha}} \end{aligned} \tag{7}$$

As depicted in Fig.4, $C_\alpha\left(x_{C_\alpha}, y_{C_\alpha}, z_{C_\alpha}\right)$ can be expressed in terms of I_α as:

$$\begin{cases} x_{C_\alpha} = x_{I_\alpha} - \left(l_{I_\alpha C_\alpha} \cos \angle A_1 E_\alpha I_\alpha\right) \\ y_{C_\alpha} = y_{I_\alpha} \\ z_{C_\alpha} = z_{I_\alpha} - \left(l_{I_\alpha C_\alpha} \sin \angle A_1 E_\alpha I_\alpha\right) \end{cases} \tag{8}$$

Through formulae (1)-(8), the location of C_α can be obtained. The z axis of the coordinate system on the point C_α is defined as the direction of the vector $\overrightarrow{O_\alpha C_\alpha}$ along the radius direction. The rotation angle of the coordinate system on the point C_α along the Y direction β_{C_α} should be

$$\beta_{C_\alpha} = \frac{\pi}{2} - \angle I_\alpha O_\alpha J_\alpha = \frac{\pi}{2} - \theta_{C_\alpha} \tag{9}$$

Generally, the location $C_\alpha\left(x_{C_\alpha}, y_{C_\alpha}, z_{C_\alpha}\right)$ is coupled to the β_{C_α}, with the vector satring from O_α to C_α as $\overrightarrow{O_\alpha C_\alpha}$ and unit vector along the X axis as $\overrightarrow{n_X}$, the relationship between them should be

$$\frac{\pi}{2} - \left\langle \overrightarrow{O_\alpha C_\alpha}, \overrightarrow{n_x} \right\rangle \tag{10}$$

Hence, this robotic arch is anticipated to encompass three DoFs. However, the homogeneous transformation matrix between the original coordinate O and the coordinate on the endpoint of SFM C_α should be

$$\begin{bmatrix} \cos\beta_{C_\alpha} & 0 & \sin\beta_{C_\alpha} & x_{C_\alpha} \\ 0 & 1 & 0 & y_{C_\alpha} \\ -\sin\beta_{C_\alpha} & 0 & \cos\beta_{C_\alpha} & z_{C_\alpha} \\ 0 & 0 & 0 & 1 \end{bmatrix} \tag{11}$$

The inverse kinematics of the proposed robotic arch will be discussed in the following sub-section. The desired endpoint of SFM C'_α is $\left(x'_{C_\alpha}, y'_{C_\alpha}, z'_{C_\alpha}\right)$ in Cartesian coordinate system, thus the original point of the arch plane O'_α consisting of desired points is $\left(0, y'_{C_\alpha}, 0\right)$. Therefore, the distance of the arch should move along the sliding rails is

$$d'_{J_\alpha} = d'_{K_\alpha} = y'_{C_\alpha} \tag{12}$$

As depicted in Fig.4, the positions (input angles in Polar coordinate system) of the legs of SFM $\angle A'_1 O'_\alpha J'_\alpha$ as θ'_{A_1} and $\angle A'_2 O'_\alpha J'_\alpha$ as θ'_{A_2} also need to be obtained. The central angle $\angle A'_1 O'_\alpha A'_\alpha$ is set as θ'_α, and $\angle C'_\alpha O'_\alpha J'_\alpha$ is set as θ'_{C_α}. The angle θ'_{C_α} will be

$$\theta'_{C_\alpha} = \left\langle \overrightarrow{O'_\alpha C'_\alpha}, \overrightarrow{n_x} \right\rangle \tag{13}$$

Additionally,

$$\angle A'_i O'_\alpha J'_\alpha (i = 1, 2) = \theta'_{C_\alpha} \pm \frac{\theta'_\alpha}{2} \tag{14}$$

According to the chord length formula $L = 2R\sin\alpha$, where the α is the central angle. The relationship between the $l_{A'_1 A'_2}$ and θ'_α will be

$$\theta'_\alpha = \arcsin \frac{l_{A'_1 A'_2}}{2R} = \arcsin \frac{2l_{A'_1 I'_\alpha}}{2R} \tag{15}$$

In addition, according to the geometrical relationship in triangle $\triangle A'_1 O'_\alpha I'_\alpha$, the relationship should be with

$$l^2_{A'_1 I'_\alpha} = R^2 - l^2_{I'_\alpha O'_\alpha} \tag{16}$$

Also,

$$l_{I'_\alpha O'_\alpha} = l_{I'_\alpha C'_\alpha} + \left|\overrightarrow{O'_\alpha C'_\alpha}\right| \tag{17}$$

Similar to (7), the relationship between the $l_{A'_1 I'_\alpha}$ and $l_{I'_\alpha C'_\alpha}$ according to the geometric relationships in SFM is

$$\begin{aligned} l_{I'_\alpha C'_\alpha} &= \sqrt{l^2_{F'_\alpha C'_\alpha} - \frac{l^2_{E'_\alpha F'_\alpha} l^2_{A'_1 I'_\alpha}}{l^2_{A'_\alpha E'_\alpha}}} \\ &+ l_{E'_\alpha F'_\alpha} \sqrt{1 - \frac{l^2_{A'_1 I'_\alpha}}{l^2_{A'_\alpha E'_\alpha}}} \\ &+ \sqrt{l^2_{A'_\alpha E'_\alpha} - l^2_{A'_1 I'_\alpha}} \end{aligned} \tag{18}$$

By simultaneous formulae (16)-(18), the $l_{A'_1 I'_\alpha}$ is able to obtain, where the $l_{F'_\alpha C'_\alpha}$, $l_{E'_\alpha F'_\alpha}$, and $l_{A'_\alpha E'_\alpha}$ are the length of linkages of SFM. When the $l_{A'_1 I'_\alpha}$ is calculated, by considering the formula (15), the θ'_α will get, then, according to (14), the angles $\angle A'_1 O'_\alpha J'_\alpha$ as θ'_{A_1} and $\angle A'_2 O'_\alpha J'_\alpha$ as θ'_{A_2} will be calculated. In addition, considering the (12), the input to the robotic arch $\left(d'_{K_\alpha}, \theta'_{A_1}, \theta'_{A_2}\right)$ will be calculated. However, multiple solutions might exist for the input to the proposed robotic arch. The following solution conditions are added according to the actual motion of the proposed robotic arch to reduce the multiple solutions.

$$\begin{cases} l_{A'_1 I'_\alpha} > 0 \\ \theta'_{A_1} < \theta'_{A_2} \\ \theta \in (0°, 180°) \end{cases} \tag{19}$$

C. Workspace Analysis and Fabrication

The workspace of the proposed robotic arch in the 70 cm MRI scanner is presented in Fig. 5. In the space analysis of the 60 cm MRI scanner, the distance between the skin of patients and the wall of the MRI scanner is about 20 cm [11]. Therefore, within a 70 cm MRI scanner, we estimate this distance to be 25 cm. Consequently, the arch of the proposed robotic arch occupies around 12% of the rest of MRI space, while the workspace is $14204.8\left(cm^3\right)$. In addition, the folding distance achieved by the SFM is around 119 mm,

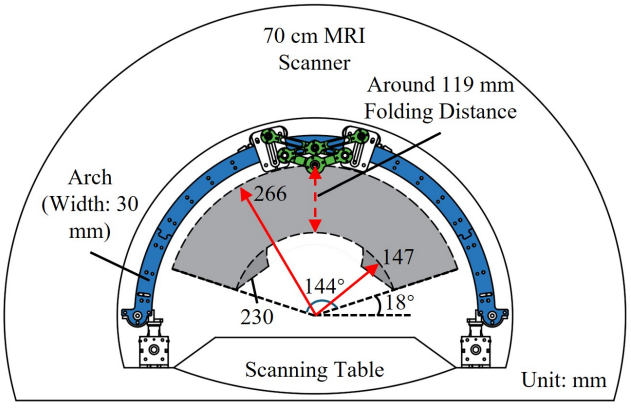

Fig. 5: Workspace of the robotic arch in MRI scanner

which is approximately 50% of the distance between the skin and the wall of the MRI scanner.

Fabrication of the robotic arch and SFM involves mainly laser cutting and 3D printing, as detailed in Tab. I, where the main components and their manufacturing methods are presented. A commercial laser cutting system, Universal VLS 4.60 (Universal Laser Systems, Inc., Scottsdale, AZ, US), was used to cut the acrylic sheets for the parts of the robotic arch. Several connectors and supports are 3D printed with a Form 3 printer (Formlabs, Inc., Boston, MA, US) and with an Ultimaker printer (Ultimaker B.V., Geldermalsen, Netherlands) according to the size and printing accuracy requirements of the parts. Ceramic, polyether ether ketone (PEEK) (JZN Bearing Co., Ltd. Shanghai, China), and xiros® polymer bearings (igus® GmbH, Cologne, Germany) are employed on the joints of the SFM to reduce friction in terms of the stress conditions on the joints of the robotic arch. The actuation for this proposed robotic arch is a modified version of the pneumatic motor presented in [16], [19] and developed by one of the authors.

D. Development of Needle Insertion Robot

Based on the above robotic arch and SFM, a novel 5-DoFs parallel robot is proposed. As depicted in Fig.6, this proposed robot featured two robotic arches with SFM and an offset needle manipulator coupled with the distal joint of the SFM of each robotic arch. There are two revolute joints in this offset needle manipulator. With the movement of two distal joints from the corresponding SFM, the end effector (needle manipulator) is steered to complete 5-DoF motion.

TABLE I: Materials and fabrication of robotic arch

Compoents	Materials and products	Approaches
Arch	Acrylic	Laser cutting
Carriage	Acrylic PLA Silicone	Laser cutting 3D prinitng Mould
SFM	Acrylic PLA	Laser cutting 3D prinitnng
Sliding rail	Acrylic	Laser cutting
Other components	Acrylic PLA, resin	Laser cutting 3D prinitnng
Commercial components	Plastic/Ceramic bearings, Nylon/PEEK blot, etc.	

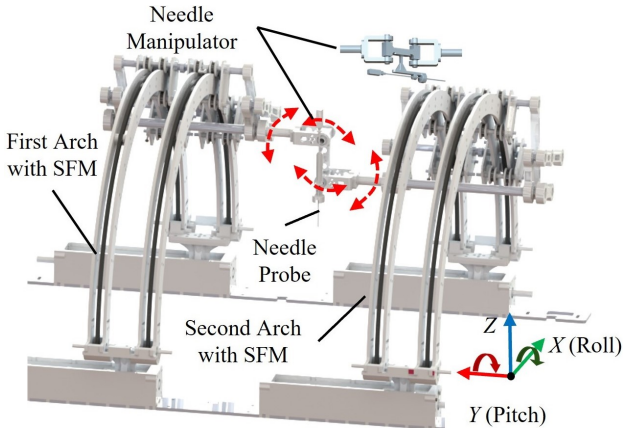

Fig. 6: Overview of the robot and its components

An overview of the degrees of freedom of the proposed needle-steering robot is presented in Fig.7. The lower offset bar of the needle manipulator connecting to the second robotic arch is always set below the offset coupled with the first robotic arch. Specifically, Fig.7 (a) illustrates the scenario that manipulates the needle to move along the Y direction. This is achieved by synchronously controlling the two robotic arches so that they move at the same speed and direction along their corresponding sliding rails. Fig.7 (b) depicts the translational movements of the needle along both the X axis and Z axis. As for the individual robotic arch, the slide of the carriages along the arch and the distance change between two sets of carriages together contribute to the change of location of the distal joint of SFM. This synergistic motion of the different groups of carriages from those two arches performs the location change of the connecting points between the SFM and offset bar of the needle manipulator. Therefore, those two DoFs are realised through the cooperation of four sets of carriages on both arches. Take the motion along the X direction as an example, and this DoF needs the sets on the first and second arches to slide in the same direction. At the same time, the distance between each of the two sets of carriages on the relative arch also needs to vary to meet the distance change along the radial direction. Compared with the translation of the needle, the rotation of the needle is accomplished via the motion synthesis from different axes. The needle roll is shown in Fig.7 (c). The axis of the roll is the axis of the joint, i.e. the hinge. This DoF is realised through the cooperation between the arch sliding along the corresponding rails, and the SFM opening and closure to meet the variation of distance in the radial direction of the arch. Fig.7 (d) shows the needle pitch. This DoF is achieved thanks to the cooperation between X and Z direction in the corresponding sets of carriages.

III. Experiments and Results

A. MRI Compatibility Experiment

A 70-cm wide bore Philips 3.0 T Ingenia MRI scanner (Philips Healthcare, Best, Netherlands) at University College

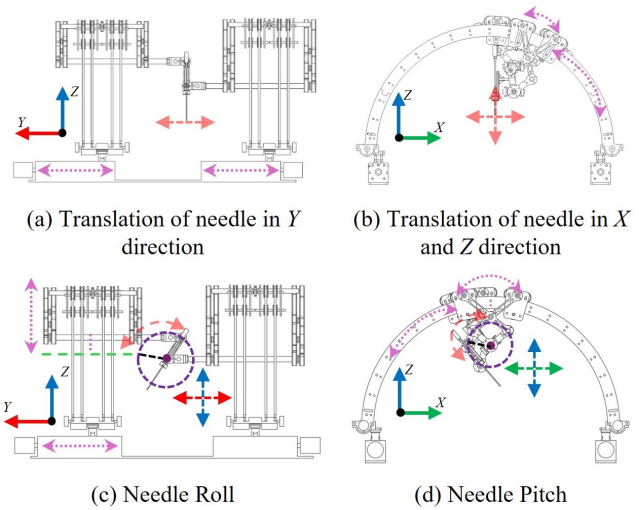

(a) Translation of needle in Y direction

(b) Translation of needle in X and Z direction

(c) Needle Roll

(d) Needle Pitch

Fig. 7: Overview of the DoFs of the needle insertion robot

Hospital Macmillan Cancer Centre was used to conduct the MRI compatibility evaluation for the robot. The three liquid phantom bottles used for the MRI test were placed on the scanning table as the scanning objects. Scanning parameters were adapted from an MRI-guided abdominal biopsies research [20] for these experiment sections. Two loop coils are on the top and bottom of the phantom bottles, respectively to enhance the image quality. The experiments were grouped into four sections: 1) Baseline Scanning (BS): This part was conducted without the robot, which was set as the standard reference for the image quality evaluation. 2) Scanning for Robot (static) (SRS): In this section, the proposed table-mounted robot is fixed to the scanning table and positioned into the MRI scanning bore. An MRI scan without activating the robot was obtained to test the influence to the images. 3) Scanning for Robot (dynamic) (SRD): Subsequently, the pneumatic motors started to drive the robot to move, and meanwhile, the scanning was collected. 4) Scanning for Robot with Abdominal Phantom (SRAP): A triple modality abdominal phantom 057A (Sun Nuclear, Melbourne, FL, US) was positioned in the MRI scanner with the proposed robot.

B. Positioning Accuracy Experiment

This evaluation experiment was carried out to evaluate the relative motion accuracy performance of the individual robotic arch and of the overall robot. The experiment setup is shown in Fig. 8. The Aurora NDI, electromagnetic tracking system (Waterloo, Ontario, Canada), was adopted for this experiment. The experiment involves two evaluations: one assessing the accuracy of the robotic arch and another examining the movement precision of the robot. The Aurora flat reference disc, as a coordinated reference, was fixed at the original point of the robotic arch and robot. In the first test for the robotic arch, another Aurora flat reference disc was screwed to the centre point of the distal joint of SFM. A tracked needle was inserted into the needle holder in the robot experiment. The experimental protocol entails providing the motor with rated pulse signals to the motor to activate the robotic arch/robot along a set path. Target points during the motion trajectory are uniformly spaced along various routes. The robotic arch/robot is controlled to traverse these points sequentially before returning to the origin. Each experiment is repeated five times. In addition, there is a tailored protractor fabricated by the laser cut integrated into the arch and sliding rails so that the sliding angle of the carriages can be obtained, as well as the distance travelled by the arch. The theoretical points are calculated according to the kinematics of the robotic arch and the input pulse of the motors, and the Aurora collects the actual points of the needle tip (red dot) and the centre point of the distal joint of SFM (green dot) of the robotic arch and the developed robot. The Euclidean distance between the theoretical and actual points is defined as movement errors.

C. Results of MRI Compatibility Experiment

Fig. 9 demonstrates the T2-weighted image results of the four MRI scans. The signal-to-noise ratio (SNR) is employed to assess the impact of the robot on the imaging. The same central rectangular section of each image is designated as the region of interest (ROI), while the corners of the image are identified as areas for noise assessment. The baseline scan set as a reference, the SNR variation of those scans with the proposed robot is less than 1.3 %. This indicates that the proposed robotic arch and developed robot do not cause obvious artefacts in the image.

D. Results of Positioning Accuracy Experiment

Fig. 10 (a) demonstrates the mean errors of positioning accuracy experiments of the proposed robotic arch with SFM (see Fig. 8). The average error of points across the five experiments is around 3.14 mm, and the variance is 2.44 mm. Fig. 10 (b) demonstrates the results of positioning accuracy experiments of the proposed robot. The average error of points along the trajectory is around 2.23 mm, and the variance is 1.41 mm.

IV. DISCUSSIONS AND CONCLUSIONS

The stringent MR safe standards require meticulous selections of materials and actuation mechanisms for the proposed

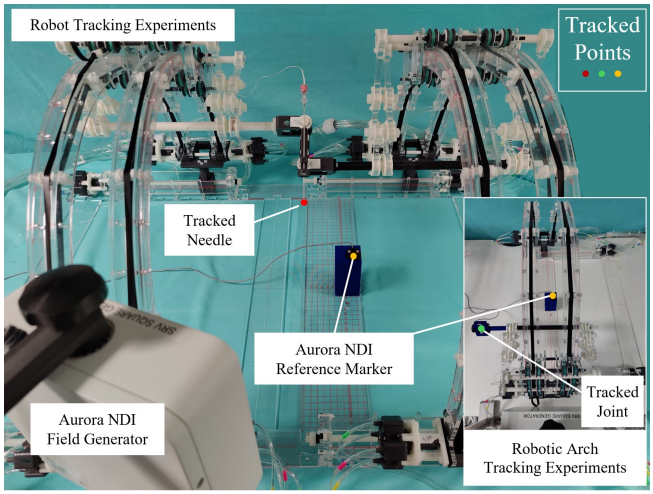

Fig. 8: Setup for positioning accuracy evaluation experiment

robot, presenting significant challenges. Plastics and ceramics emerge as viable materials for constructing these type of robotic systems. However, their mechanical strengths might not rival those of metals, necessitating careful consideration to ensure the stability of the robot. Therefore, a robust structural design is adopted, featuring a dual-structure approach with arches, scissor-folding mechanisms, and carriages to enhance connectivity and minimise part deformation. Despite this, the inherent limitations of material strength could lead to operational vibrations in certain components of the robot. Nonetheless, such minor oscillations fall within the acceptable margin for the clinical application. Moreover, the distributed arrangement of multiple pneumatic motors acts as a redundancy strategy, ensuring sufficient torque for each movement while minimising the torque demand on individual motors. However, challenges remain in maintaining the air tightness for the pneumatic motors to deliver the required torque, particularly in systems with inevitably long and multiple pipes that can lead to air pressure loss.

During the positioning accuracy experiment of the robotic arch, especially in the final linear path movement, there was a cumulative error among the points of under 6 mm (maximum 5.98 mm) in the worst-case scenario. This primarily stemmed from the slight deformation of the acrylic base beneath the sliding rails due to the motion of the sliders. However, considering the fabrication approaches of those prototypes, enhancements in movement precision are anticipated with the application of high-precision fabrication techniques, such as CNC machining. Further improvements in accuracy could be achieved by integrating sensors within the robot system, enabling a closed-loop control strategy to mitigate error accumulation. Therefore, in the experiment assessing the positioning accuracy of the robot, theoretical points are

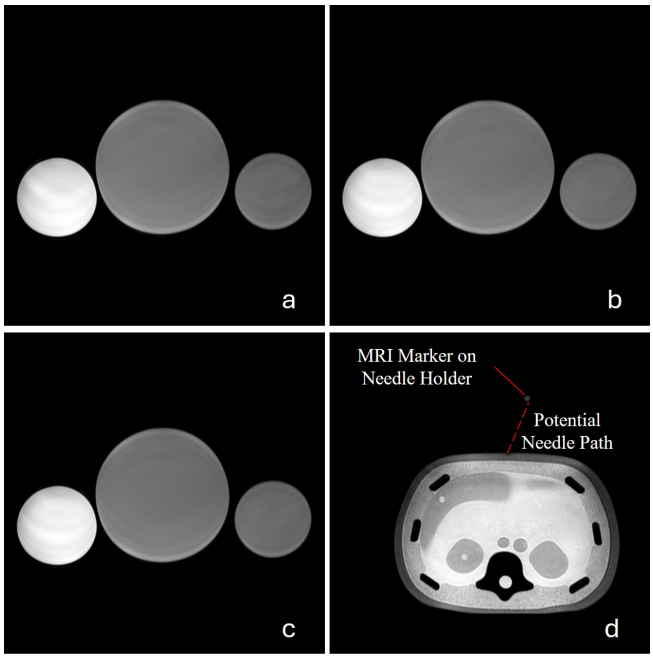

Fig. 9: Results of the MRI compatibility experiments (a): BS (b): SRS (c): SRD (d): SRAP

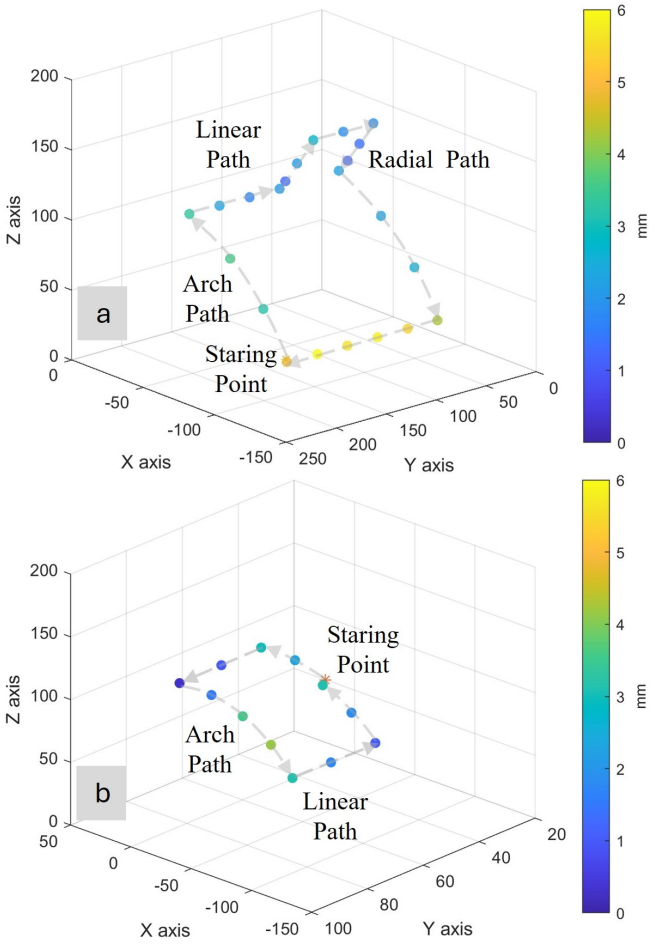

Fig. 10: Results of the positioning accuracy experiment: point-to-point errors in the robotic arch movement (a), and in the overall robot movement (b)

derived from the preceding one to gauge the relative motion precision of the robot, disregarding the potential for error accumulation from several points. The mean errors are 2.23 mm, with minimum average errors of 0.29 mm between the fourth and fifth points, highlighting the capability of the robot for highly accurate movements over short distances. Systematic evaluations of the robot to analyse its capabilities across various scenarios will be conducted in the foreseeable future, and an exploration into the application of visual servo will also be explored.

The kinematic principles of the proposed modular robotic arch with SFM were elaborated. Utilising this adaptable design, a variety of configurations are possible, such as integrating a multi-jointed arm with the distal joint of the robotic arch or positioning an offset needle manipulator adjacent to one of the dual arches, and middle configuration demonstrated in this paper. The kinematics vary across these setups, warranting systematic exploration of their complete kinematic analyses in future discussions. However, the actuation methods of the multi-jointed arm need to be considered to avoid interference among the joints, as well as the weight and size for the first configuration. The primary challenges should be the deformation of the long beam connecting

the needle manipulator to the second robotic arch and the interference between it and the SFM. The optimal approach would be the current configuration that puts the needle manipulator between two frames.

The folding travel distance of the current SFM mechanism along the radial direction is approximately 119 mm. However, for interventions involving long needles in clinical practice, it is necessary to optimise the trajectory to avoid collision with the wall of the MRI scanner according to the figure of the patient and target location during the surgery. In addition, sterilisation and the avoidance of interference with other medical instruments should be considered in the clinical application. Further work will also involve enhancing the performance of the robot for clinical interventions.

In summary, a novel table-mounted MR safe 5-DoF parallel robot based on modular robotic arches with SFM was proposed. The carriages coupled to the SFM can slide along the arch, which can also slide on the rails. The designed robotic arch with SFM can accomplish around 119 mm folding distances in the 70 cm MRI scanner, which is the 50% distance between the scanner wall and the skin of the patient. Furthermore, the developed robot consists of two robotic arches and a needle manipulator to realise 5 DoFs through the coordination of those two robotic arches, corresponding carriages on the arches to steer the needle manipulator connected to the distal joints of the relative SFMs so that the position and pose of the needle probe can be changed. The initial evaluation suggests that the proposed robotic arch and the robot exhibit an average relative motion precision of 3.14 mm and 2.23 mm, respectively, and the effect resulting from the robot on the MRI imaging could be negligible.

ACKNOWLEDGMENT

The authors would like to thank the senior research radiographer, Julia Markus, from the Faculty of Medical Sciences, University College London, who conducted those MRI scans for the robot, and Alistair Lamb, from the Centre for Medical Imaging, University College London, who also gave us suggestions in the data processing aspect.

REFERENCES

[1] World Health Organization, "Cancer Today," 2022. [Online]. Available: https://gco.iarc.fr/today/en/dataviz/pie?mode=cancer&group_populations=1&types=1&show_table_pie=1

[2] Word Cancer Research Fund International, "Kidney cancer statistics," 2022. [Online]. Available: https://www.wcrf.org/cancer-trends/kidney-cancer-statistics/

[3] C. R. Weiss, S. G. Nour, and J. S. Lewin, "MR-guided biopsy: A review of current techniques and applications," *Journal of Magnetic Resonance Imaging*, vol. 27, no. 2, pp. 311–325, 2 2008.

[4] S. Okamoto, *et al.*, "Needle artifact characteristics and insertion accuracy using a 1.2 T open MRI scanner: A phantom study," *Diagnostic and Interventional Imaging*, vol. 102, no. 6, pp. 363–370, 2021.

[5] A. Öcan and N. Tsekos, "The interconnection of MRI scanner and MR-compatible robotic device: Synergistic graphical user interface to form a mechatronic system," *IEEE/ASME Transactions on Mechatronics*, vol. 13, no. 3, pp. 362–369, 6 2008.

[6] E. Franco, D. Brujic, M. Rea, W. M. Gedroyc, and M. Ristic, "Needle-guiding robot for laser ablation of liver tumors under MRI guidance," *IEEE/ASME Transactions on Mechatronics*, vol. 21, no. 2, pp. 931–944, 4 2016.

[7] N. Hungr, I. Bricault, P. Cinquin, and C. Fouard, "Design and Validation of a CT-and MRI-Guided Robot for Percutaneous Needle Procedures," *IEEE Transactions on Robotics*, vol. 32, no. 4, pp. 973–987, 8 2016.

[8] N. Hata, R. Hashimoto, J. Tokuda, and S. Morikawa, "Needle guiding robot for MR-guided microwave thermotherapy of liver tumor using motorized remote-center-of-motion constraint," in *IEEE International Conference on Robotics and Automation (ICRA)*, vol. 2005, 2005, pp. 1652–1656.

[9] Z. He, *et al.*, "Design of a Percutaneous MRI-Guided Needle Robot with Soft Fluid-Driven Actuator," *IEEE Robotics and Automation Letters*, vol. 5, no. 2, pp. 2100–2107, 4 2020.

[10] N. Zemiti, I. Bricault, C. Fouard, B. Sanchez, and P. Cinquin, "LPR: A CT and MR-compatible puncture robot to enhance accuracy and safety of image-guided interventions," *IEEE/ASME Transactions on Mechatronics*, vol. 13, no. 3, pp. 306–315, 2008.

[11] E. G. Christoforou, I. Seimenis, E. Andreou, E. Eracleous, and N. V. Tsekos, "A novel, general-purpose, MR-compatible, manually actuated robotic manipulation system for minimally invasive interventions under direct MRI guidance," *International Journal of Medical Robotics and Computer Assisted Surgery*, vol. 10, no. 1, pp. 22–34, 3 2014.

[12] A. N. Alvara, T. Looi, R. Saab, A. Shorter, A. Goldenberg, and J. Drake, "Development and Validation of MRI Compatible Pediatric Surgical Robot with Modular Tooling for Bone Biopsy," in *IEEE International Conference on Intelligent Robots and Systems (IROS)*, 12 2018, pp. 4935–4941.

[13] N. A. Patel, J. Yan, D. Levi, R. Monfaredi, K. Cleary, and I. Iordachita, "Body-Mounted Robot for Image-Guided Percutaneous Interventions: Mechanical Design and Preliminary Accuracy Evaluation," in *IEEE International Conference on Intelligent Robots and Systems (IROS)*, 12 2018, pp. 1443–1448.

[14] J. Yan, N. Patel, G. L. Di Wu, K. Cleary, and I. Iordachita, "Body-Mounted MRI-Conditional Parallel Robot for Percutaneous Interventions Structural Improvement, Calibration, and Accuracy Analysis," in *Annual International Conference of the IEEE Engineering in Medicine and Biology Society (EMBC)*, 7 2019, pp. 1990–1993.

[15] American Society for Testing and Materials, "ASTM F2503-20, Standard Practice for Marking Medical Devices and Other Items for Safety in the Magnetic Resonance Environment," 2023. [Online]. Available: https://compass.astm.org/document/?contentCode=ASTM%7CF2503-20%7Cen-US&proxycl=https%3A%2F%2Fsecure.astm.org&fromLogin=true

[16] V. Groenhuis and S. Stramigioli, "Rapid Prototyping High-Performance MR Safe Pneumatic Stepper Motors," *IEEE/ASME Transactions on Mechatronics*, vol. 23, no. 4, pp. 1843–1853, 2018.

[17] H. Ranjan, *et al.*, "Sunram 7: An MR Safe Robotic System for Breast Biopsy," in *IEEE International Conference on Intelligent Robots and Systems (IROS)*, 2023, pp. 10 281–10 288.

[18] E. Mendoza and J. P. Whitney, "A Teleoperated MR-Safe Haptic System for Magnetic Resonance Imaging-Guided Prostate Needle Biopsies," in *IEEE International Conference on Intelligent Robots and Systems (IROS)*, 2023, pp. 5122–5127.

[19] M. E. Abdelaziz, *et al.*, "Toward a Versatile Robotic Platform for Fluoroscopy and MRI-Guided Endovascular Interventions: A Pre-Clinical Study," in *IEEE/RSJ International Conference on Intelligent Robots and Systems (IROS)*, 2019, pp. 5411–5418.

[20] J. P. Kühn, *et al.*, "Magnetic resonance-guided upper abdominal biopsies in a high-field wide-bore 3-T MRI system: Feasibility, handling, and needle artefacts," *European Radiology*, vol. 20, no. 10, pp. 2414–2421, 2010.